### Title

Determination of the optimal camera distance for cloud height measurements with two all-sky imagers




### Authors

Kuhn, P
Nouri, B
Wilbert, S
et al.



### Publication Date

2019-02-01

### DOI

10.1016/j.solener.2018.12.038

Peer reviewed

# Determination of the optimal camera distance for cloud height measurements with two all-sky imagers

P. Kuhn[1,*]

*German Aerospace Center (DLR), Institute of Solar Research, Ctra. de Senés s/n km 4, 04200 Tabernas, Spain.*

B. Nouri[1], S. Wilbert[1], N. Hanrieder[1], C. Prahl[1], L. Ramirez[2], L. Zarzalejo[2], T. Schmidt[3], T. Schmidt[4], Z. Yasser[5], D. Heinemann[3], P. Tzoumanikas[6], A. Kazantzidis[6], J. Kleissl[7], P. Blanc[8], R. Pitz-Paal[9]

**Abstract**

All-sky imager based systems can be used to measure a number of cloud properties. Configurations consisting of two all-sky imagers can be used to derive cloud heights for weather stations, aviation and nowcasting of solar irradiance. One key question for such systems is the optimal distance between the all-sky imagers. This problem has not been studied conclusively in the literature. To the best of our knowledge, no previous in-field study of the optimal camera distance was performed. Also, comprehensive modeling is lacking.

Here, we address this question with an in-field study on 93 days using 7 camera distances between 494 m and 2562 m. We model the findings and draw conclusions for various configurations with different algorithmic approaches and camera hardware.

The camera distance is found to have a major impact on the accuracy of cloud height determinations. For the used 3 megapixel cameras, cloud heights up to 12000 m and the used algorithmic approaches, an optimal camera distance of approximately 1500 m is determined. Optimal camera distances can be reduced to less than 1000 m if higher camera resolutions (e.g. 6 megapixel) are deployed. A step-by-step guide to determine the optimal camera distance is provided.

*Keywords:* All-sky imagers, cloud height measurements, solar nowcasting

*Corresponding author

*Email address:* Pascal.Kuhn@dlr.de (P. Kuhn)

[1]German Aerospace Center (DLR), Institute of Solar Research, Ctra. de Senés s/n km 4, 04200 Tabernas, Spain.

[2]CIEMAT, Energy Department - Renewable Energy Division. Av. Complutense, 40, 28040 Madrid, Spain.

[3]German Aerospace Center (DLR), Institute of Networked Energy Systems, Carl-von-Ossietzky-Straße 15, 26129 Oldenburg, Germany.

[4]CSP Services GmbH, Friedrich-Ebert-Ufer 30, 51143 Cologne, Germany.

[5]TSK FLAGSOL, Cologne, Anna-Schneider-Steig 10, 50678 Cologne, Germany.

[6]Laboratory of Atmospheric Physics, Department of Physics, University of Patras, 26500 Patras, Greece.

[7]Dept. of Mechanical and Aerospace Engineering, UCSD Center for Energy Research, University of California, 92093-0411 La Jolla, USA.

[8]MINES ParisTech, PSL Research University, Centre Observation, Impacts, Energy (O. I. E.), CS 10207, F-06904, Sophia Antipolis CEDEX, France.

[9]German Aerospace Center (DLR), Institute of Solar Research, Linder Höhe, 51147 Cologne, Germany.

## 1. Introduction

Cloud heights are of interest for energy meteorological applications such as the nowcasting of solar irradiance (Nouri et al. (2017), Chu et al. (2017)), weather services (e.g. Campbell et al. (2018), Müller et al. (2018)) and aviation (Wiegmann et al. (2002), Mecikalski et al. (2007)), where cloud height is critical for non-instrument flight operations. All-sky imager based systems can provide such cloud height measurements. In comparison to ceilometers, they are less expensive, can provide multiple cloud heights at once and are not confined to a point-like measurement area above the instrument. In recent years, many approaches to determine cloud heights based on two (or more) all-sky imagers were published (see Tab. 1).

Due to the low installation and maintenance costs, all-sky imager configurations with two cameras are especially relevant. Moreover, in Kuhn et al. (2018b), such a configuration is found to be the most promising one out of five different cloud height providing systems. A key question for such systems is the optimal distance between the cameras. This question is addressed here. The answer to that question depends on a multitude of chosen hardware and software parameters.

To the best of our knowledge, the question of the optimal camera distance was not previously studied with in-field studies. Furthermore, in most publications listed in Tab. 1, the used camera distance is not specifically motivated or studied, but seems to be imposed by local availability. In the following, we briefly summarize previous works relevant for this study.

Using cameras with a similar resolution (1748×1748 pixels) as the cameras used here and a distance of 1230 m, Nguyen and Kleissl (2014) derive that clouds at 2627 m can be optimally measured and the configuration is reliable up to 5250 m. These values are derived by looking at the change of the overlap between the cameras' viewing cones ($\Delta$Overlap, change in the sky area seen by both cameras) in relation to the change in cloud height. A threshold of $\frac{\Delta\text{Overlap}}{\Delta\text{cloud base height}} = \frac{0.1\ \%}{100\ \text{m}}$ is chosen for *"demonstration purposes"* and not further motivated. The dependency on the camera resolution is not studied. However, the interplay between cloud heights and the optimal camera distance is identified.

In Massip et al. (2015), a stereographic sensitivity [pixel/m] study is conducted for four of the five cameras used here, including a study on the directional dependencies on a 4 $km^2$ area and a cloud base height of 3000 m. The stereographic sensitivity can be derived from the camera resolution and the parallax in pixel caused by an altitude variation of the cloud height in [m]. *"For limited variation of altitude (less than 500 m), this stereoscopic sensitivity is linearly increasing"* with decreasing cloud height. A direct translation of these findings into an optimal camera distance is difficult. However, Massip et al. (2015) highlight the anisotropy and sensitivity of cloud height measurements, raising the related question of the best orientation of a two camera system for given local conditions such as prevailing wind direction. This question is briefly addressed in section 5.

Katai-Urban et al. (2018) model the challenges of camera-based cloud height derivations and address

Table 1: Camera distances and resolutions used for cloud height measurements as published in literature.

| **Reference** | **Camera distance** | **Camera resolution** |
|---|---|---|
| de WA (1885) | 410 m | theodolites (human eye) |
| Strachey and Whipple (1891) | 730 m | analog camera |
| Kassander and Sims (1957) | 2100 m | analog camera |
| Orville and Jr. (1961) | 4820 m | analog camera |
| Allmen and Kegelmeyer Jr (1996) | 5540 m | 256×256 pixels (indicated in Johnson et al. (1989)) |
| Kassianov et al. (2005) | 540 m | 352×288 pixels |
| Seiz et al. (2007) | 850 m | 3060×2036 pixels / 3072×2048 pixels |
| Damiani et al. (2008) | not specified | 2048×1536 pixels |
| Hu et al. (2009) | 1500 m | 2048×1536 pixels |
| Janeiro et al. (2012) | 28.9 m | 3888×2592 pixels |
| Urquhart et al. (2012) | 1800 m | 640×480 pixels |
| Nguyen and Kleissl (2014) | 1230 m | 1750×1750 pixels |
| Öktem et al. (2014) | 1000 m | 1296×960 pixels / 1024×768 pixels |
| Andreev et al. (2014) | 17 m | 3072×2304 pixels |
| Peng et al. (2015) | 2477 m / 956 m | 640×480 pixels |
| Roy (2016) | 590 m | 2560×1920 pixels |
| Beekmans et al. (2016) | 300 m | 2448×2048 pixels |
| Katai-Urban et al. (2016) | 90 m | 5184×3456 pixels |
| Savoy et al. (2017) | 100 m | 5184×3456 pixels |
| Blanc et al. (2017) | 572 m | 2048×1536 pixels |
| Katai-Urban et al. (2018) | 90/100/130 m | 5184×3456 pixels |

the question of the optimal camera distance for cloud heights between 1000 m and 2000 m. They find that for the applied approaches, using a camera resolution of 5184×3456 pixels, cloud height deviations decrease up to a camera distance of 200 m. Beyond a camera distance of 200 m, little improvements are found. Without further explanation, optimal camera distances between 2000 m and 10000 m for cloud heights between 1000 m and 5000 m are indicated in Katai-Urban et al. (2016), also stating that such large distance would *"show too much geometric and photometric distortion, which makes the matching of cloud pixels unfeasible"* (Katai-Urban et al. (2016)).

Our approach to address the question of the optimal camera distance for cloud height measurements with two all-sky imagers is twofold:

(1) We present an in-field study with various camera distances within a two camera configuration (section 2). In this study, cloud heights derived from configurations with different camera distances are compared to cloud base heights measured by a ceilometer. (2) In a second step, we model the expected cloud height deviations as a function of the camera distance to determine the optimal distance and compare the results to the finding of the field study (section 3).

Usually, camera-based cloud height measurements approaches rely on cloud segmentation or locating common points of interest within images, which might be, according to Bernecker et al. (2013), a main origin of errors. To reduce hardware dependencies and increase the robustness, a cloud segmentation-independent approach to derive cloud heights from two all-sky imagers is developed in Kuhn et al. (2018b). This approach is explained in the next section and used here.

In section 4, we attempt to extrapolate the findings to different camera hardware. The distances between the cameras are not only relevant for the accuracy of cloud height measurements, but also for other aspects. For instance, large distances between cameras lead to a larger area of the sky being imaged by the multi-camera system. Such considerations will be discussed in section 5. A step-by-step guide to define relevant parameters is included in section 6. The conclusion is given in section 7. This study is motivated by the industrial and practical relevance as well as by the variety of different camera distances used in the literature (see Tab. 1).

To summarize our findings, a list of parameters that impact the optimal camera distance is given here in decreasing importance: (1) cloud height itself, (2) camera resolution, (3) minimum viewing angle, (4) cloud positions in relation to the image geometry and (5) cloud positions in relation to the cameras' axis.

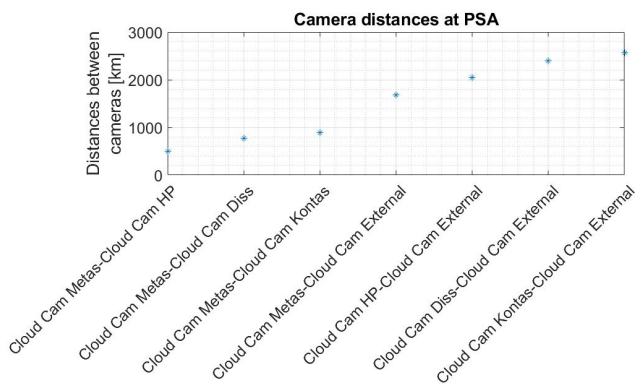


(a) Camera distances at PSA.

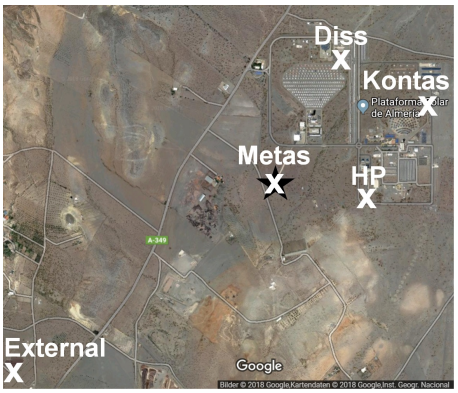


(b) Cameras' positions at PSA: White x mark the cameras' positions and the black star marks the position of the ceilometer. [googlemaps]

Figure 1: Cameras' positions and distances at the Plataforma Solar de Almería (PSA).

## 2. In-field study of cloud heights derived by two all-sky imagers at different camera distances

### *2.1. Approach, settings and configurations*

This study is conducted using five all-sky imagers and seven camera distances on the Plataforma Solar de Almería (PSA) in southern Spain. The positions of the cameras are indicated in Fig. 1. The minimum distance is 494 m, the maximum distance is 2562 m. Although there is a gap between 890 m and 1679 m, the distances are well distributed and, as of 2017, globally unique for such a study (see Fig. 1). The all-sky imagers have a resolution of 3 megapixel (MP) and are off-the-shelf surveillance cameras (Mobotix, Q24 at Metas, HP and Diss as well as Q25 at Kontas and External).

Pairs of two cameras are used to calculate the cloud height as described in and with the same parameters of Kuhn et al. (2018b). This approach is briefly summarized here and shown in Fig. 2. To derive a cloud height, two images from both cameras, taken 30 s apart, are subtracted ($d_i(x, y)$ in Fig. 2) and projected into one orthoimage for each camera ($o_i(m, n)$). These difference orthoimages are segmented into binary images ($b_i(m, n)$) by using a dynamic threshold (98th percentile). The binary images are then matched, deriving a cloud speed in [pixel/s]. This so-called *matching distance* between the orthoimages is a key parameter and corresponds to the known distance of the camera. This allows the conversion of the matching distance from [pixel/s] to [m/s]. With both the angular and the absolute velocity derived, one general cloud height for each timestamp is calculated for the whole image.

This approach is independent from cloud detection algorithms, which reduces dependencies on camera hardware. For instance, Q24 and Q25 cameras and different camera chips are used together in this study. The exterior and internal orientations of the cameras, however, must be known. The used orthoimages have a resolution of 1000×1000 pixels ($N \times N$). In principle, this resolution could be increased. However,

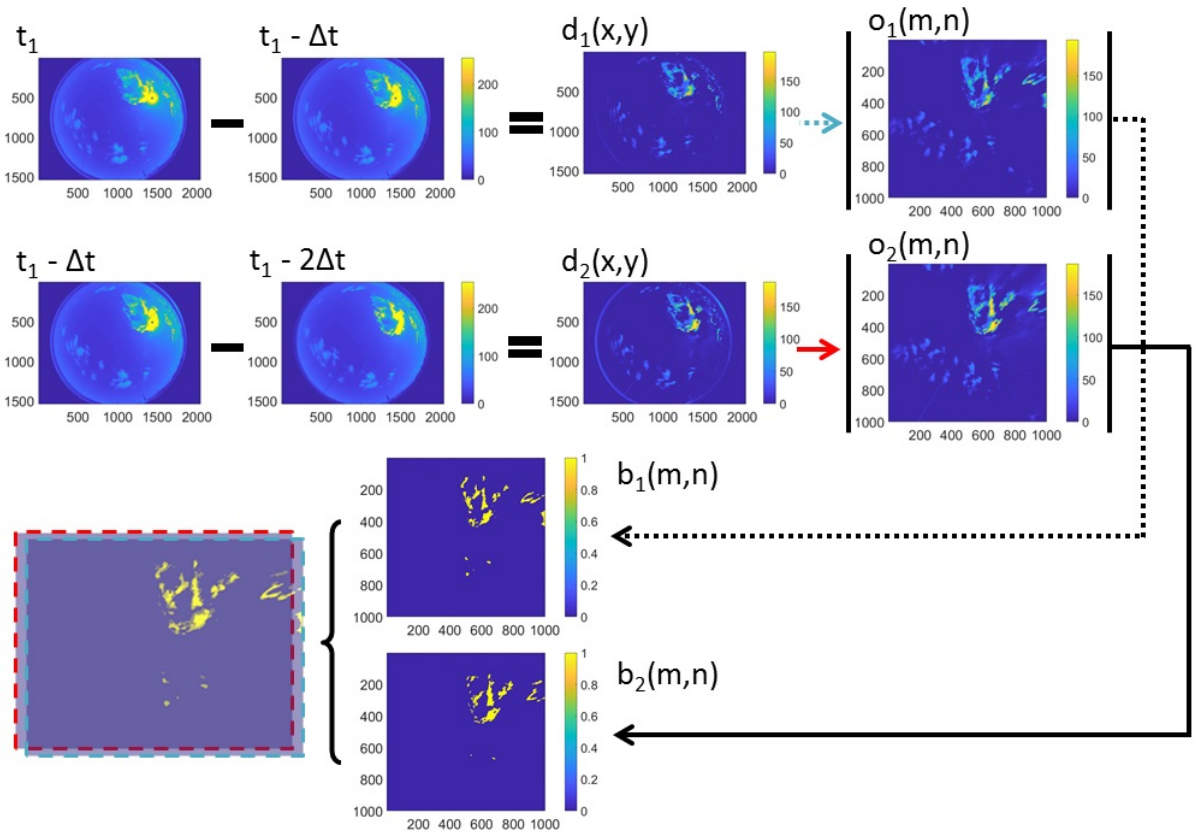


Figure 2: Working principle of the cloud height derivation using two all-sky imagers (adapted from Kuhn et al. (2018b)).

due to the limited amount of pixels on the cameras' chips, this increase would not yield more physical information. The minimum elevation angle $\alpha = 12^{\circ}$ is the minimum angle present in the orthoimage for all azimuth angles. In the edges, smaller elevation angles are projected into the orthoimage, which is considered to be of minor importance in this study. Figure 3 visualizes these parameters.

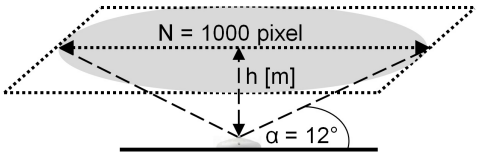


Figure 3: Sketch showing the properties of the orthoimage (adapted from Kuhn et al. (2018b)).

Conventional deviation metrics such as root-mean-square deviations (RMSD), standard deviation (std), mean-absolute deviations (MAD) and bias (equ. 1-4) on 10 min gliding medians are used to quantify the deviations between the all-sky imager derived cloud heights ($h_{\text{ASI-ASI,i}}$) and the ceilometer

cloud base heights ($h_{\text{ceilometer,i}}$).

$$\text{bias} = \frac{1}{N}\sum_{i=1}^{N}(h_{\text{ASI-ASI,i}} - h_{\text{ceilometer,i}}) \tag{1}$$

$$\text{std} = \sqrt{\frac{1}{N}\sum_{i=1}^{N}\left((h_{\text{ASI-ASI,i}} - h_{\text{ceilometer,i}}) - \text{bias}\right)^2} \tag{2}$$

$$\text{RMSD} = \sqrt{\frac{1}{N}\sum_{i=1}^{N}(h_{\text{ASI-ASI,i}} - h_{\text{ceilometer,i}})^2} \tag{3}$$

$$\text{MAD} = \frac{1}{N}\sum_{i=1}^{N}|h_{\text{ASI-ASI,i}} - h_{\text{ceilometer,i}}| \tag{4}$$

Cloud heights as measured by the ceilometer and the cloud heights measured by the all-sky imager systems are not identical: Ceilometers measure cloud base heights directly above the position of the instrument. On the other hand, the all-sky imager based approach used here is more likely to measure a mean cloud height of optically thick clouds. Also, ceilometers can show "*a considerable degree of scatter*" (Martucci et al., 2010) and comparisons found an average bias of 160 m (Martucci et al., 2010) or 50 m (Gaumet et al., 1998) between two ceilometers. Nonetheless, we consider the ceilometer used here (CHM 15k NIMBUS, G. Lufft Mess- und Regeltechnik GmbH) to be a valid reference.

The evaluation is conducted for periods during which the ceilometer measured a temporally relatively constant cloud height. This limitation is needed to avoid multiple cloud height situations. These situations are excluded as the ceilometer conducts point-like measurements whereas the all-sky imager systems determine the heights of clouds causing the largest difference in the difference images (see Fig. 2). In situations, in which both optically thick cumulus clouds and optically thin ice clouds are present, the all-sky imager configurations thus tend to derive the height of the (usually lower) cumulus clouds. As clouds are often seen from the side, the measured cloud height is not considered to be the cloud bottom height as provided by the ceilometer, but a mean height of these clouds. Therefore, in multi-layer conditions, systematic deviations between the camera-derived and the ceilometer measurements are present, which are not the subject of this study. Thus, multi-layer cloud situations are excluded.

The periods of temporally relatively constant cloud heights are manually pre-selected by looking for constant cloud height conditions in ceilometer measurements. In a second step, timestamps for which the ceilometer measures a standard deviation in cloud base heights larger than 30 % relative to the ceilometer mean cloud base height measurements within a period of 3 h (90 min around each timestamp) are excluded. Moreover, only timestamps for which all systems derived a cloud height are included in the comparison. This leads to a total of 39491 timestamps on 93 days.

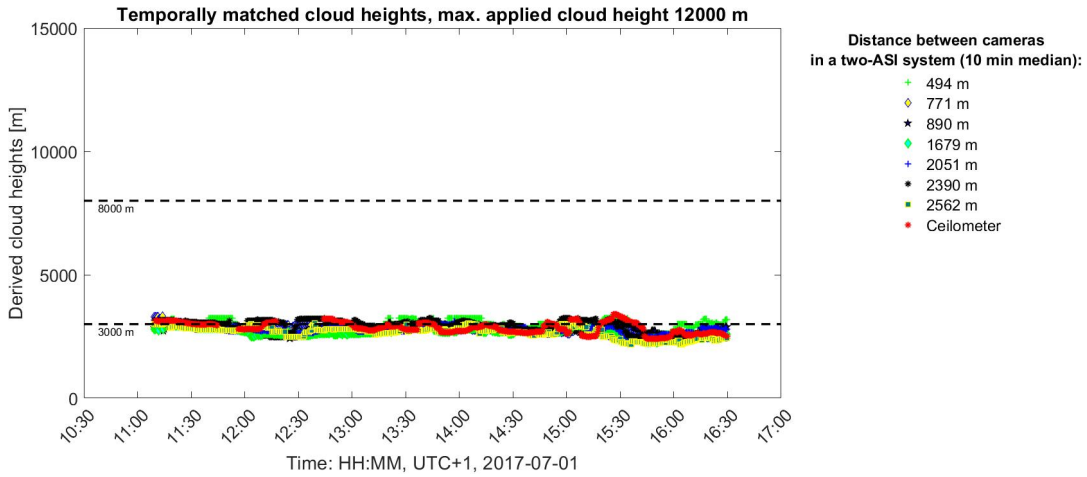


Figure 4: Raw data of all-sky imager derived cloud heights in comparison to ceilometer cloud base heights on 2017-07-01.

### *2.2. Experimental results of the in-field study on cloud heights using different camera distances*

We specifically look at the raw data of three of the 93 days to highlight certain effects. The first day, 2017-07-01, is shown in Fig. 4. Throughout the selected period of time, a constant cloud height of 3000 m is present, which is accurately measured by all configurations. On 2017-01-19, shown in Fig. 5, the ceilometer also measures a relatively constant cloud height at about 2000 m. However, configurations with large camera distances show significant deviations.

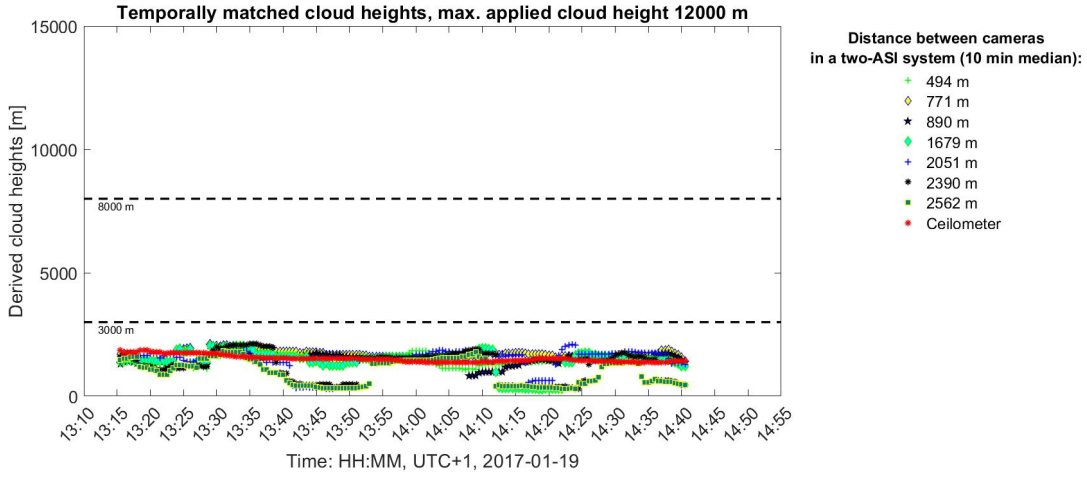


Figure 5: Raw data of all-sky imager derived cloud heights in comparison to ceilometer cloud base heights on 2017-01-19.

Figure 6 depicts the cloud heights measured during a selected period on 2017-05-29. During that period, the ceilometer measures a constant cloud height at about 7000 m. Configurations with small camera distances of 494 m and 890 m often over-estimate this cloud height, with overshootings being present especially for the setup with the smallest distance. The configuration with the camera distance

of 771 m, however, does not show such overshootings.

Larger camera distances of 1679 m, 2051 m, 2390 m and 2562 m derive cloud heights similar to the ceilometer cloud heights between 17:00 h and 17:50 h. Between 16:20 h and 16:45 h, these setups measure lower cloud heights than the ceilometer. During this period, high ice clouds are present over the ceilometer. The all-sky imager, however, also image lower cumulus clouds (see Fig. 7). Due to the differential approach of the all-sky imager setups, such cumulus clouds are more likely to be matched as optically thin ice clouds. Therefore, the all-sky imager derived cloud heights of approximately 2000 m might be physically correct. The ramp visible in Fig. 6 at approximately 16:50 h is caused by the 10 min gliding median applied to the all-sky imager derived cloud heights.

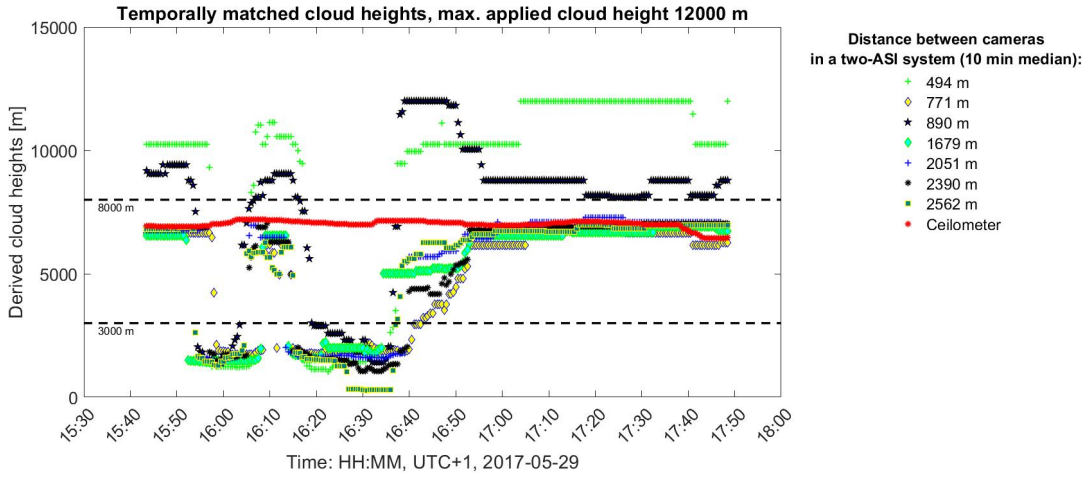


Figure 6: Raw data of all-sky imager derived cloud heights in comparison to ceilometer cloud base heights on 2017-05-29.

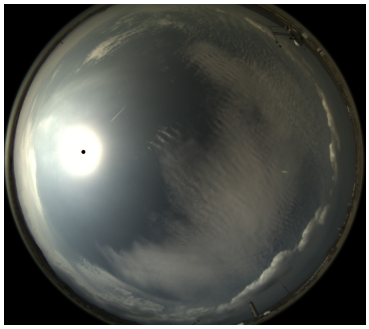

Figure 7: Fisheye all-sky image taken by the Metas camera on 2017-05-29 16:45:00 UTC+1. Both high clouds (image center) and lower clouds (e.g. bottom right edge) are visible. The ceilometer measures base heights of clouds visible in the center of this image.

For the following comparisons, cloud heights are called "low" if the ceilometer measures a height at or below 3000 m. "High" cloud heights correspond to ceilometer measurements at or above 8000 m. "Medium" cloud heights correspond to ceilometer measurements between 3000 m and 8000 m.

All-sky imager derived cloud heights above 12,000 m are set to this maximum cloud height. The applied maximum cloud height is introduced to physically limit the all-sky imager derived cloud heights and does not affect ceilometer measurements.

The deviations are displayed in Fig. 8 for low, medium and high clouds as well as all considered camera distances. The number of measurements used in this comparison for all system is 18927 for low clouds, 14935 for medium clouds and 5629 for high clouds.

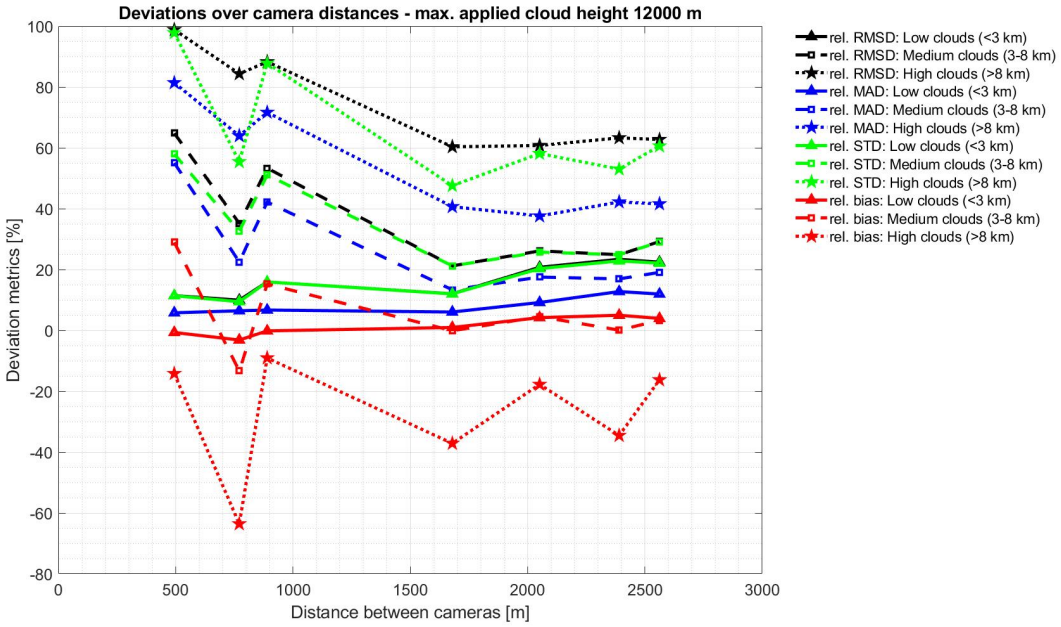


Figure 8: Derived cloud height deviations on 93 days using 7 camera distances. The number of measurements for low clouds is 18927, for medium clouds 14935 and for high clouds 5629.

For high clouds (dotted lines), the deviations decrease with larger camera distances: From 98.8 % RMSD for the smallest camera distance (494 m) via 60.3 % at a distance of 1679 m to 62.7 % for the maximum distance considered here (2562 m) The same holds, on a lower deviation level, for medium clouds (dashed lines, from 64.8 % RMSD via 21.2 % to 29.2 %). For low clouds (solid lines), the deviations increase with larger camera distances (from 11.4 % RMSD via 12.0 % to 22.4 %).

For high clouds, the second smallest distance (771 m) sticks out with a significant negative bias. This bias is not present for this distance for low and medium clouds, for which this distance is more accurate than similar distances.

The MADs and the standard deviations show trends similar to those of the RMSD with a tendency to decrease for larger camera distances and high clouds as well as to increase for larger camera distances and low clouds. For high clouds, the MAD decreases from 81.4 % (494 m) to 37.6 % (2051 m) and 41.6 % (2562 m). For medium clouds, the MAD decreases from 55.1 % (494 m) to 19.1 % (2562 m). For low

clouds, the MAD increases from 5.8 % (494 m) to 11.9 % (2562 m).

The standard deviation drops for high clouds from 97.8 % (494 m) to 60.6 % (2562 m) with a minimum of 47.6 % for a camera distance of 1679 m. For medium cloud heights, the standard deviation decreases from 58.0 % (494 m) to 29.0 % (2562 m) with a minimum of 21.2 % for 1679 m. For low clouds, the standard deviation increases from 11.4 % (494 m) via 9.4 % (771 m) and 22.8 % (2390 m) to 22.1 % (2562 m).

In Fig. 8, we see two distinct trends: (1) For medium and high clouds, the deviations shrink with larger camera distances up to 1679 m. For camera distances beyond 1679 m, no major improvements of the metrics are found. (2) For low clouds, the deviations increase with larger camera distances.

To further study the impact of different camera distances, scatter density plots of each configuration are shown in Fig. 9a-9g. The scatter density plots visualize the cloud height deviations found between the all-sky imager configuration and the reference ceilometer.

Fig. 9a shows the scatter density plot for the smallest camera distance (494 m). This configuration is able to accurately derive cloud heights up to approximately 2500 m. Greater cloud altitudes are measured with a significant amount of scatter. Many clouds, measured by the ceilometer to have heights between 11000 m and 12000 m, are determined by this configuration to have heights of about 2000 m. This could be an indication that not every multi-layer cloud situation is filtered out. As the filtering is only conducted on the data of the ceilometer reference, clouds not being measured by the ceilometer could cause this effect. In such situations, the ceilometer might determine the altitude of a high cloud directly above the instrument whereas the all-sky imager system may measure a general height of other clouds in the sky. As highlighted with Fig. 7, this could explain a certain amount of the artefacts seen in the scatter density plots (Fig. 9a-9g).

In Fig. 9b, the scatter density plot corresponding to a camera distance of 771 m is presented. This system measures cloud heights up to approximately 3000 m with better accuracy for cloud heights between 3000 m and 5000 m compared to the 494 m system. The scatter at higher altitudes is biased, meaning that the system underestimates cloud heights more frequently than overestimations occur. This is reflected in the large negative bias shown in Fig. 8.

The configuration with a camera distance of 890 m is depicted in Fig. 9c. In contrast to the very similar distance of 771 m, shown in Fig. 9b, the scatter is not biased towards lower estimations. However, for cloud heights above 2500 m, cloud heights cannot be accurately determined. Fig. 9d shows the configuration with the overall best accuracy, having a camera distance of 1679 m. Low, medium and high cloud heights are derived with less scatter in comparison to other distances. For larger camera distances (Fig. 9e-9g), the scatter increases in comparison to the results of the camera distance of 1679 m.

Figure 10 shows the standard deviations of the configurations relative to ceilometer cloud base heights for a bin size of 200 m. Corresponding to Fig. 8 and 9, we see that small camera distances (solid lines)

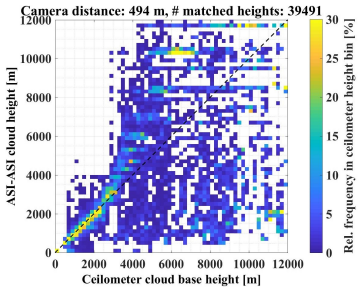


(a) Camera distance: 494 m

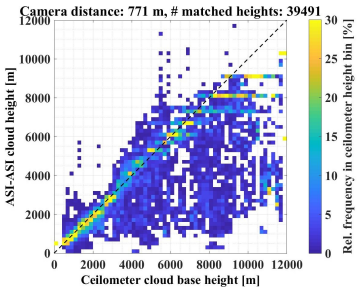


(b) Camera distance: 771 m

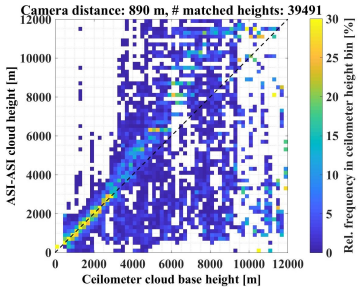


(c) Camera distance: 890 m

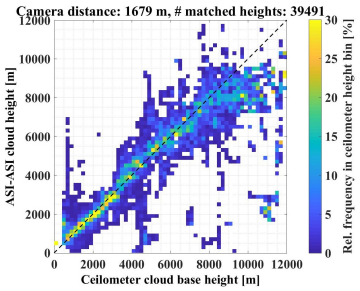


(d) Camera distance: 1679 m

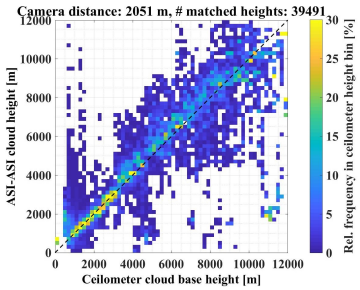


(e) Camera distance: 2051 m

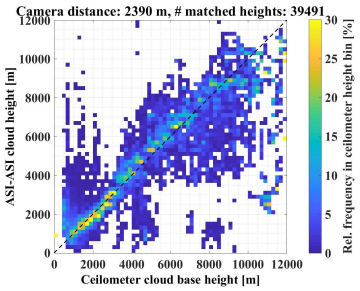


(f) Camera distance: 2390 m

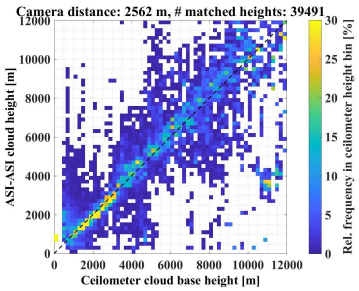


(g) Camera distance: 2562 m

Figure 9: Scatter density plot for cloud heights on 93 days derived by two all-sky imagers and various camera distances. Cloud heights derived from both the all-sky imagers and the ceilometer are compared with a bin size of 200 m. The color shows the relative frequency of the temporally matched cloud heights within each ceilometer cloud height bin. This means that the relative frequencies in one column, which is one ceilometer cloud height bin, add up to 100 %. The results are displayed again for 10 minute medians derived from the all-sky imager systems and compared to 10-minute median measurements of the ceilometers.

scatter less than large camera distance (dotted lines) for low cloud heights, but scatter more for high clouds. Beyond 10000 m, the scatter is similar for all camera distances, which is contributed to the discussed multi-layer situations.

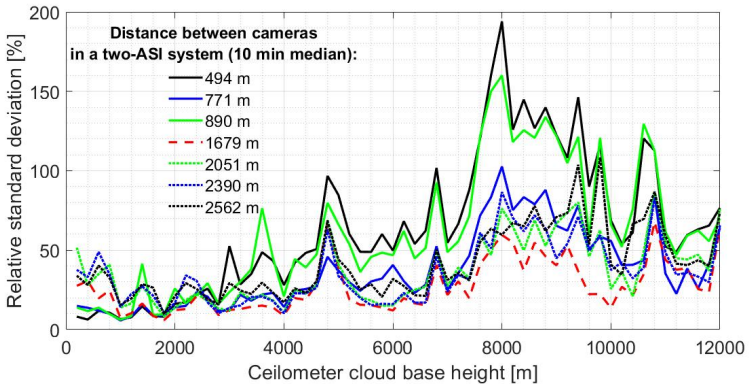


Figure 10: Standard deviation relative to ceilometer cloud base height for all considered all-sky imager systems (bin size: 200 m).

## 3. Modeling the findings of the in-field study

### *3.1. Explaining deviations for small distances and high clouds*

In order to study the overshooting effects visible e.g. in Fig. 6 and Fig. 9a for small camera distances and high clouds, we study a specific timestamp. This timestamp is 2017-08-04, 13:47:00 UTC+1. For this timestamp, the ceilometer measures a cloud height of 11613 m. The two all-sky imager system with a camera distance of 1678 m derives a cloud height of 10353 m, the system with 494 m camera distance calculates a non-physical cloud height of 53066 m (53 km). The derived cloud velocity [pixel/s] of both systems is the same: $\Delta y = 0$ pixel/30 s and $\Delta x = -1$ pixel/30 s. The same velocity in [pixel/s] derived from $d_1(x, y)$ and $d_2(x, y)$ in Fig. 2 leads, due to the different camera distances, to distinctly different cloud velocities of 3.2 m/s (for a camera distance of 1678 m) and 16.4 m/s (for the camera distance of 494 m) and hence to the high deviation in the derived cloud heights (10353 m and 53066 m). The reason for this mismatch is the lack of camera resolution in the matching of the difference images: For the camera distance of 494 m, a matching distance of a fraction of a pixel in the orthoimages would result in the ceilometer cloud height. Due to discretization, this is not possible. Setups using small camera distances thus undersample pixel-resolution-wise clouds at high altitudes, resulting in scatter.

In Fig. 11, the relation between matching distances between the orthoimages of the cameras ($b_1(x, y)$ and $b_2(x, y)$ in Fig. 2, see section 2.1 for explanations) and the ratio of cloud heights and camera distances is shown. A matching distance of 10 pixels is present if the cloud heights are 10.6 times higher than the

219 camera distance. The matching distance is 51 pixels if this ratio is 2.1 and drops to 2 if the cloud height are 53.1 times larger than the camera distance.

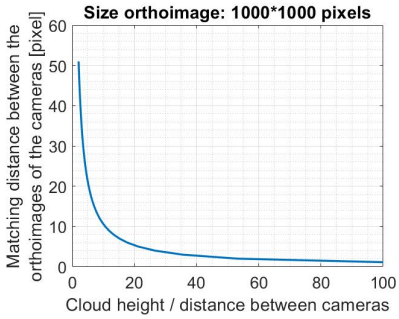


Figure 11: Matching distance between the orthoimages of the cameras in pixel over the ratio of cloud height and camera distance. If the cameras are in close proximity relative to the cloud heights to be measured, the matching distance is small and mismatches / under-sampling occurs.

220

221 Figure 11 is derived using equ. 5, which is based on equ. 4 in Kuhn et al. (2018b). In equ. 5, $s_{match}$
222 is the matching distance, $N$ is the size of the orthoimage in one dimension, $\alpha$ is the minimum viewing
223 angle, $h$ is the height of the cloud layer and $D$ the distance between the cameras.

224 $$s_{match} = \frac{N}{2 \cdot \tan(90° - \alpha)} \cdot \frac{1}{h/D} \tag{5}$$

225 Figure 12 shows the corresponding cloud height errors divided by the camera distance. A minor
226 mismatch of one singular pixel has a stronger impact on the expected accuracy if the ratio between cloud
227 height and camera distance is large.

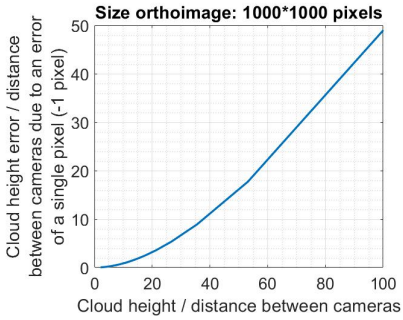


Figure 12: Cloud height errors divided by camera distance caused by a mismatch of one pixel over the ratio of cloud height and camera distance (corresponding to Fig. 11): For small ratios, the such mismatches impact the accuracy stronger than for larger ratios.

228 The undersampling effect shown in Fig. 11 and 12 for large ratios affects the configurations with
229 camera distance below 1000 m (Fig. 9). This effect is biased for the setup with a camera distance of
230 771 m towards lower cloud heights. Furthermore, this setup shows little deviations in comparison to
231 ceilometer measurements for certain periods shown in Fig. 6. The reason for both this bias and the good

agreement on 2017-05-29 remains unclear, but due to the lack of physical information (undersampling) for high clouds, we opt to not consider this any further.

### *3.2. Explaining deviations for large distances and low clouds*

In section 2.2, deviations and scatter are found to increase with increased camera distances for low cloud heights. The reason for this is explained by the concept of overlap. If the cameras are further apart, the overlap of the cameras' viewing cones is reduced (Fig. 13). Clouds which are not located inside this overlapping volume are only seen by one camera (or none). The heights of such clouds cannot be determined. In general, increasing the camera distance reduces the matching area, which makes mismatches more likely.

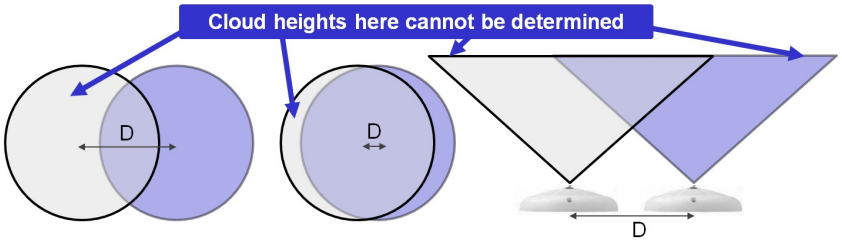


Figure 13: Small distances between the cameras lead to large overlaps. If the cameras are further apart (larger camera distance $D$), the overlap is reduced.

The overlap depends on the ratio of cloud heights and camera distances as shown in Fig. 14. For instance, for a ratio of 1 (same cloud height and camera distance, e.g. 2 km), the overlap is 86.5 %. If the cloud height is 4 times greater than the camera distance, the overlap increases to 96.6 %. Similarly, a ratio of 0.5 results in an overlap of 73.1 %. If the camera distance is 5 times larger than the cloud height (ratio of 0.2), the overlap is further reduced to 35.7 %. As a comparison, EKO Instruments (2018) suggests a ratio of 5 (overlap: 97.3 %) to 7 (overlap: 98.1 %) for optimal accuracy.

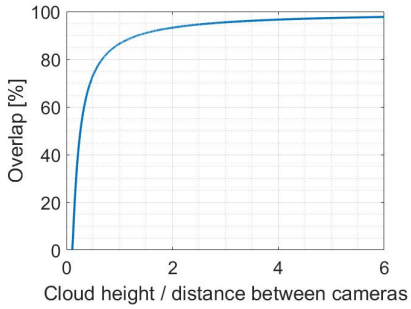


Figure 14: Overlap between two cameras in relation of ratios of cloud heights over camera distances.

Figure 14 is derived using equ. 6. In equ. 6, $R$ is the radius of the viewing cone with $R = h/\tan(\alpha)$

($h$: cloud layer height; $\alpha$: minimum viewing angle) and $D$ is the distance between the cameras.

$$\text{Overlap} = \frac{2 \cdot R^2 \cdot \arccos(D/(2 \cdot R)) - 0.5 \cdot d \cdot \sqrt{4 \cdot R^2 - D^2}}{\pi \cdot R^2} \cdot 100\% \tag{6}$$

## 4. Impacts of the camera hardware and parameters on the optimal camera distance

In this section, we link our findings to camera hardware and settings, which enables a limited generalization and extrapolation to other setups. Section 4.1 considers the impacts of the camera resolution on the optimal distance. The effects of the minimum viewing angle $\alpha$ are studied in section 4.2. Section 4.3 briefly discusses the influence of the cloud positions within the all-sky image geometry. The impacts of the image acquisition rate are presented in section 4.4.

### *4.1. Relation between camera resolution and optimal distance*

The resolution of the camera is considered to be the most relevant parameter for this study. Janeiro et al. (2012), utilizing a camera distance of only 28.9 m, use for instance a high resolution of 3888×2592 pixels.

In the study presented here, the orthoimage has a resolution of 1000×1000 pixels. The orthoimage is derived from raw fisheye images and can be set to have a higher resolution. However, due to the lack of information, this artificially higher resolution does not come with higher accuracy. The used all-sky imagers (Mobotix Q24 and older Q25 models) have a resolution of 3 MP. Higher resolution fisheye cameras, e.g. with 12 MP or more, are available.

With this physically higher resolution, orthoimages with a higher resolution can be employed. For instance, the orthoimage could be $\gamma = \frac{2048}{1536} = 1.\overline{3}$ larger if a 6 MP (2048×3078) camera instead of a 3 MP camera (1536×2048) is used. This camera resolution is applied in the new camera model Mobotix Q25, which is used in Nouri et al. (2017). Hypothetically, the orthoimage can therefore be enlarged by the factor $\gamma$ in each direction while containing the same average physical information per pixel (more detailed calculations are presented in the next sections). This would linearly increase the matching distance between the cameras' orthoimages ($y$-axis in Fig. 11) by a factor of $\gamma' = \gamma \cdot \mathrm{M}$, $\mathrm{M} = \{x | 1 \leq x \leq \sqrt{2}\}$ (depending on the direction of the matching, diagonal or along the edges of the orthoimage). This factor has a non-linear impact of $1/\tan(\gamma')$ on the accuracy (see Fig. 11 and 12). Thus, higher camera resolutions reduce the required camera distances. This behavior is partially reflected in the distances and resolutions summarized in Tab. 1.

### *4.2. Minimum viewing angle $\alpha$ and optimal camera distance*

The minimum viewing angle considered so far is $\alpha = 12°$. Several important parameters of the orthoimage depend on this angle, which will be studied here for several camera resolutions. Figure 15

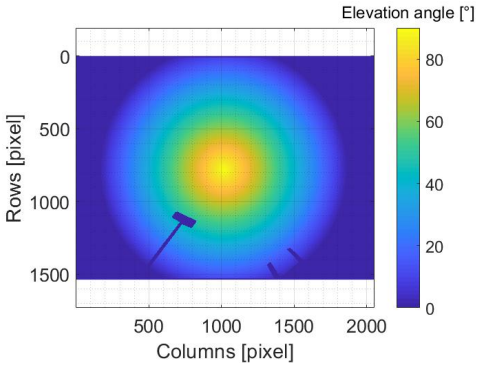


Figure 15: Elevation angles in a 3 MP fisheye raw image.

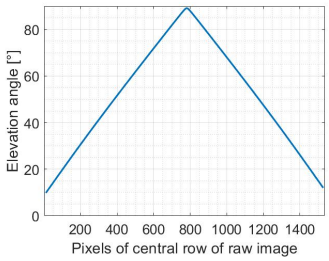


Figure 16: Elevation angles of the center row within a 3 MP fisheye raw image, corresponding to Fig. 15.

shows the elevation angles within a 3 MP raw fisheye image. In Fig. 16, where the elevation angles of the center row are depicted, we see a linear relation with a gradient of approximately $\pm 0.103^{\circ}$/pixel.

Although custom lenses exist (e.g. Gutwin and Fedak (2004), Singh et al. (2006), Schmidt et al. (2015)), we assume that the linear relation visible in Fig. 16 holds for most fisheye cameras. Assuming furthermore that the first pixel of the center row images a minimum elevation of $\theta_{min} = 0^{\circ}$ and the center pixel a maximum elevation of $\theta_{max} = 90^{\circ}$ , the gradient $\Delta\beta$ can be calculated using equ. 7. This yields a gradient of $0.117^{\circ}$/pixel for a 3 MP image (2048×1536 pixels; due to the symmetry of all-sky images, the relevant resolution value in this section is always the smaller one.). This calculated gradient is reasonably close to the gradient shown in Fig. 16.

$$\Delta\beta = \frac{\theta_{max} - \theta_{min}}{\Delta\text{pixel indices}} \rightarrow \frac{90^{\circ} - 0^{\circ}}{(0.5 \cdot 1536 - 1)\text{ pixels}} = 0.117^{\circ}/\text{pixels} \tag{7}$$

If an orthoimage is generated (see Fig. 17), the center area is compressed into relatively few pixels. On the other hand, the edge region is stretched. This stretching depends on the minimum viewing angle $\alpha$ as shown in Fig. 18.

Under the assumption of a linear elevation gradient (see equ. 7), the *physical plane-projected resolution* ($PPR$) can be calculated using equ. 8 with $\Delta\beta$ being the gradient derived in equ. 7, $n$ being the pixel distance to the center and $h$ being the cloud layer height. The $PPR$ describes the physical spatial resolution within a plane at a given height which depends on the elevation angles of the corresponding

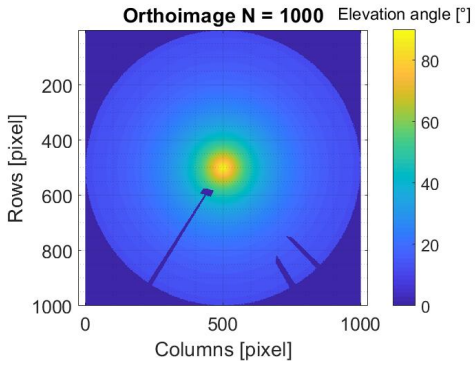


Figure 17: Elevation angles in an orthoimage with a resolution of 1000×1000 pixels and a minimum viewing angle of $\alpha = 12°$, corresponding to Fig. 15. Small minimum viewing angles may lead to extrapolations caused by the lack of physical information.

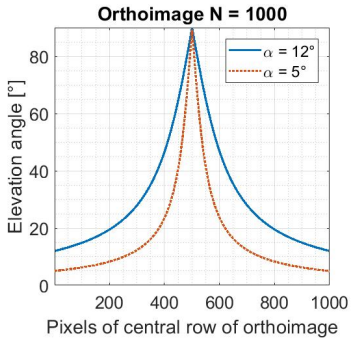


Figure 18: Elevation angles of the center row within an orthoimage with a resolution of 1000×1000 pixels ($N \times N$) and two minimum viewing angles, corresponding to Fig. 15. Smaller minimum viewing angles result in stronger compression of the center area and stretching of the raw fisheye image's edges.

pixels in the raw fisheye image. A visual explanation of the parameters is given in Fig. 19. Figure 20 shows the relation between elevation angles, camera resolutions and the physical plane-projected resolutions, normalized by the cloud height.

$$PPR = h \cdot \big(\tan(n \cdot \Delta\beta) - \tan((n-1) \cdot \Delta\beta)\big) \tag{8}$$

We derive from Fig. 20 that a minimum viewing angle of $\alpha = 12°$ corresponds to a $PPR$ normalized by the cloud height of 0.047 for a camera resolution of 1536 pixels and to a normalized $PPR$ of 0.021 for a camera resolution of 3456 pixels. For a cloud layer height of 5000 m, this corresponds to a minimum physical plane-projected resolution of 231.4 m and 104.1 m, respectively. These minimum resolutions hold for the minimum viewing angle. If we allow such edge pixels to be extrapolated over a maximum stretching factor of e.g. $\kappa = 5$ pixels in the corresponding orthoimage, the orthoimage has a resolution of $\frac{235 \text{ m}}{5 \text{ pixels}} = 46.3$ m/pixel or 20.8 m/pixel.

The corresponding sizes of the orthoimages are calculated using equ. 9 to be $N = 1009$ pixels and

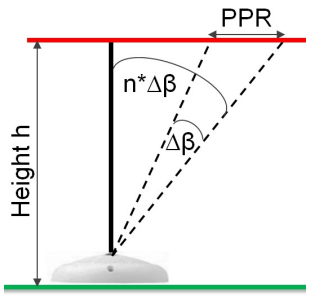


Figure 19: Visual explanations corresponding to equ. 8 and the concept of the physical plane-projected resolution ($PPR$). $\Delta\beta$ is the gradient derived in equ. 7, which depends on the camera's resolution. The normalized $PPR$ is shown in Fig. 20.

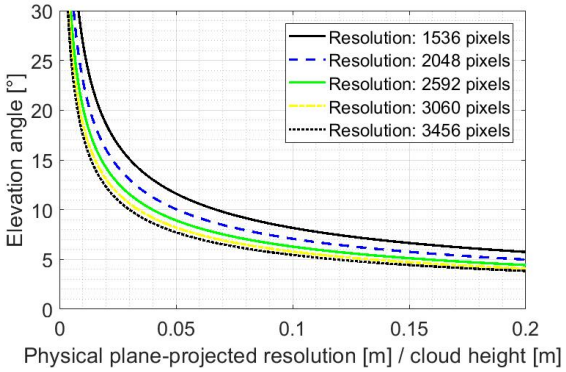


Figure 20: Physical plane-projected resolution ($PPR$) divided by cloud height shown for elevation angles and camera resolutions, derived from equ. 8.

$N = 2252$ pixels, respectively. In equ. 9, $N$ is the size of the orthoimage in one dimension, $PPR$ is the physical plane-projected resolution determined by equ. 8 and $\kappa$ is the stretching factor for the least resolved fisheye pixel in the orthoimage.

$$N = \frac{2}{\kappa} \cdot \sum_{\zeta_{ele}=\alpha}^{90^\circ} PPR(\zeta_{ele}) \tag{9}$$

For a minimum viewing angle of $\alpha = 5^\circ$, the minimum $PPR$ increases to 1293.8 m and 591.9 m. Using the same resolutions of the orthoimage as before, the orthoimages' sizes expand to $N = 4053$ pixels and $N = 4015$ pixels, with the least resolved pixel being stretched over 27.9 pixels or 28.5 pixels.

As a conclusion, a feasible minimum viewing angle must be chosen keeping the physical plane-projected resolution and the corresponding optimal size of the orthoimage in mind. Large minimum viewing angles reduce the overlap between the cameras, but are beneficial for the amount of physical information in the orthoimage. If the minimum viewing angles are small, the chosen resolution of the orthoimage may become non-physical with singular pixels from the raw image being stretched over dozens of pixels in the orthoimage, caused by the lack of physical information. This stretching makes mismatches more likely and thus reduces the expected accuracy, especially for clouds imaged far away

from the center of the all-sky images (see next section).

### *4.3. Impact of cloud positions in relation to the image geometry*

Using $\Delta\beta$ as defined in equ. 7, the vertical resolution can be calculated, e.g. for a vertical plane between the cameras as depicted in Fig. 21. This vertical resolution is specified by equ. 10 with $D$ being the distance between the cameras and $n$ the pixel distance to the center of the raw fisheye image. Equation 10 is visualized for the $\Delta\beta$ of the used cameras. With a distance between the cameras of 1500 m, the corresponding vertical resolution between the cameras at 10000 m altitude is for instance 247 m .

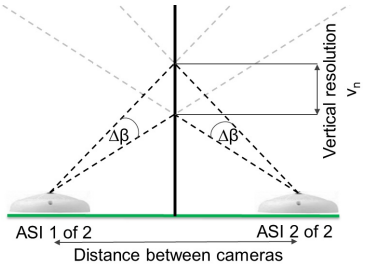


Figure 21: Vertical resolution $v_n$ for a vertical plane between the cameras. The vertical resolution can be calculated using equ. 10, leading to Fig. 22.

$$v_n = \frac{D}{2} \cdot \left(\tan(90^\circ - n \cdot \Delta\beta) - \tan(90^\circ - (n-1) \cdot \Delta\beta)\right) \tag{10}$$

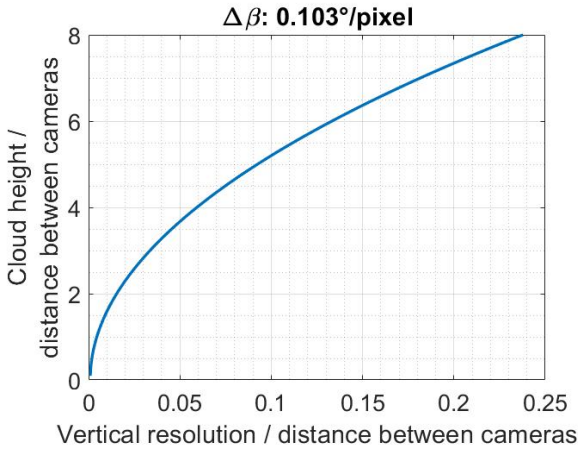


Figure 22: Vertical resolution $v_n$, calculated using equ. 10 and normalized by the distance between the cameras.

This vertical resolution is less resolved for positions far away from the cameras. Thus, the deviations of cloud height measurements depend on the position of the cloud in relation to the image center. In general, this relation could be, similar to the discussion in section 4.2, camera-specific. Besides the

reduced vertical resolution, clouds seen under small elevation angles for a camera are imaged in the distorted edge regions of the fisheye image. There, the calibration accuracy might be worse than in the center. These deviations impact the orthoimage, leading to matching deviations. These deviations depends on the cameras' calibrations and their imaging systems.

In addition to that, clouds at the edges of the fisheye all-sky images are rather seen from the side, not from the bottom. This might lead to perspective errors in certain cloud height measurement approaches (Kuhn et al., 2018a). Moreover, as discussed in section 4.2 and shown e.g. in Fig. 17, the physical resolution within the orthoimage decreases towards the edges and pixels from the fisheye raw image might be stretched over several pixels in the orthoimage. This clearly reduces the accuracy of cloud height measurements in these regions.

As many of these effects are camera-specific or depend on chosen settings, a general qualitative assessment is not conducted here. However, measured heights of clouds near the center of the images / above the cameras' positions are, based on the considerations presented in this section, estimated to be more accurate.

### *4.4. Image acquisition rate and optimal camera distance*

The temporal resolution is not considered to play a major role for the determination of the optimal camera distance. However, high temporal resolutions (e.g. 1 s) combined with limited pixel resolutions could lead to an oversampling effect. This holds for the differential approach used here, which matches differences between subsequent images. If the image acquisition rate is too high, the spatial difference in the cloud positions between two subsequent images could be below the camera resolution. In this scenario, a matching is not possible. Yet, non-subsequent images with larger temporal differences could still be used to obtain cloud heights. On the other hand, very low temporal resolutions larger than 1 min could increase matching errors due to cloud dynamics (blur effects).

Other approaches to determine cloud heights from two all-sky imagers are based on two images taken simultaneously by both cameras (e.g. Allmen and Kegelmeyer Jr (1996), Kassianov et al. (2005), Seiz et al. (2007), Nguyen and Kleissl (2014), Beekmans et al. (2016) and Blanc et al. (2017)). In these approaches, the image acquisition rate only determines the amount of measurements per unit of time and does not affect the cloud height determination itself.

## 5. Further aspects relevant for the optimal camera distance

As shown in the previous sections, the distance between the cameras of an all-sky imager system impacts its ability to accurately determine cloud heights. However, besides cloud heights, the camera distance is of importance for other parameters as well.

If, for instance, a network of relatively independent all-sky imagers shall cover an area as large as possible, the overlap should be reduced to the required minimum. The derivation of cloud height information is thus more difficult or even impossible. However, depending on the application, cloud height information might be less relevant or could be externally provided to the cameras. Such example applications are the all-sky imager based detection of solar variability classes (e.g. Stefferud et al. (2012), Nouri et al. (2018)), cloud coverage (e.g. Ackerman and Cox (1981), Tapakis and Charalambides (2013), Jayadevan et al. (2015), Dev et al. (2017), Kuhn et al. (2017)), cloud type classifications (e.g. Heinle et al. (2010), Martínez-Chico et al. (2011), Kazantzidis et al. (2012), Taravat et al. (2015), Xia et al. (2015)) or camera-derived solar irradiance measurements (e.g. Tohsing et al. (2013), Tohsing et al. (2014), Tzoumanikas et al. (2016)).

Furthermore, for certain applications, low clouds are more important than high clouds, e.g. for not instrument-rated pilots (e.g. Hunter (2002), Atsushi (2004), Fultz and Ashley (2016)). Therefore, the focus of the application has an impact on the optimal camera distance. In practice, however, maximum distances between the cameras of nowcasting systems are often defined by property boundaries or the availability of infrastructure.

A question related to the optimal camera question is the optimal orientation of the cameras, which is briefly addressed in Massip et al. (2015). Depending on the predominant cloud motion direction, the intended application and algorithmic approaches, an orientation of the two cameras' axis in parallel or orthogonal to the main cloud motion direction is preferable. An orientation orthogonal to the main cloud motion direction is, to a minor degree, superior for cloud height measurements as clouds coming from this main direction are seen by both cameras at a similar time, enabling earlier cloud height derivations for clouds with motion vectors aligned with the axis of the two cameras. If the early detection of clouds is more important than their heights, an orientation in parallel with the main cloud motion direction is more appropriate. Moreover, if a cloud field is approaching the cameras, one cloud motion vector and one cloud height could be derived from the foremost cloud and extrapolated to the whole cloud field.

## 6. Step-by-step guide to determine the optimal distance between cameras and further required parameters for all-sky imager based cloud height measurements

We start with the assumption of having two cameras with the same resolution. The cameras are further assumed to have standard fisheye lenses, which hypothetically show a linear relation between the imaged elevations and the pixels similar to Fig. 16. In the following, the relevant configuration parameters are derived step by step. This list is, to a certain degree, specific for the algorithmic approach used in this study.

1. Calculate the gradient $\Delta\beta$, adapting equ. 7 to the used camera hardware.
2. Calculate the $PPR$ using equ. 8.

3. Chose the minimum viewing angle $\alpha$ as large as possible for your application. For most applications, angles of $\alpha = \{\alpha | 10^\circ \leq \alpha \leq 30^\circ\}$ are considered to be feasible.
4. Define the minimum $PPR$/cloud height based on the minimum viewing angle $\alpha$ and equ. 8, shown in Fig. 20.
5. Chose the maximum stretching factor $\kappa$ between the fisheye raw image pixel at the minimum viewing angle and the corresponding pixel in the orthoimage. A reasonable stretching factor for these edge pixels is thought to be 5.
6. Define the cloud height $h$, which is considered most important for your application. Relevant heights could be between $h = \{h | 100 \text{ m} \leq h \leq 10 \text{ km}\}$.
7. Calculate the minimum resolution $res_{min}$ in the orthoimage with $res_{min} = PPR_{min}/\kappa$. Is this minimum resolution feasible for your application? If this is not the case, you might reconsider the minimum viewing angle $\alpha$ or the required camera resolution.
8. Calculate the optimal size $N \times N$ of the orthoimage using equ. 9.
9. Define the minimum matching distance $s_{match}$. Reasonable minimum matching distances are considered to be around 10 pixels. From this minimum matching distance and the relevant cloud height $h$, the distance between the cameras $D$ can be derived using equ. 5.
10. Control the overlap of the cameras' viewing cones with equ. 6. Arguably, this overlap should be larger than 95 % for most applications. You may also like to check the vertical resolutions at relevant distances from your setup using equ. 10.

If camera distances are defined by local infrastructure, calculate backwards to assure the feasibility or assess limitations of the imposed distance.

## 7. Conclusion

We aimed at identifying the optimal camera distance of a cloud height measurement system consisting of two all-sky imagers. An in-field study on 93 days, using 7 configurations, is presented and the findings are explained using modeling. For the used configuration and all cloud heights, an optimal camera distance of approximately 1500 m appears to be best suited. Smaller camera distances result in undersampling effects for clouds at high altitudes. Larger camera distances do not improve the deviations found for high clouds but introduce (to a minor extend) scatter, especially for low clouds. This is caused by a reduced overlap in the cameras' fields of view.

We consider the resolution of the camera the most important lever to utilize if small camera distances are needed. We estimate that camera distances below 1000 m are feasible for camera resolutions at and above 6 MP, which mostly corresponds to parameters used in the literature: For instance, Hu et al. (2009) use the same camera resolution (2048×1536 pixels) and a camera distance of 1500 m. Similar

distances and resolutions are used by Nguyen and Kleissl (2014) (1230 m, 1750×1750 pixels) and Öktem et al. (2014) (1000 m, 1296×960 pixels / 1024×768 pixels). Smaller camera distances and higher camera resolutions are used by Seiz et al. (2007) (850 m, 3060×2036 pixels / 3072×2048 pixels), Roy (2016) (590 m, 2560×1920 pixels), Beekmans et al. (2016) (300 m, 2448×2048 pixels) and Savoy et al. (2017) (100 m, 5184×3456 pixels). These combinations of camera resolution and distance are in alignment with our findings.

In Andreev et al. (2014), a camera distance of 17 m and a resolution of 3072×2304 pixels are used. Our findings indicate that this combination is only feasible for low clouds, which is confirmed in Andreev et al. (2014): The deviation estimation reaches 50 % for cloud heights of 2000 m and the authors state that the accuracy can be improved by *"increasing the distance between the cameras or use higher image resolutions"* (Andreev et al. (2014)). Janeiro et al. (2012) (28.9 m, 3888×2592 pixels) validate the obtained cloud heights on one day with two cloud layers (1500 m and 6000 m), showing good agreement to a reference ceilometer. They note that the vertical resolution for clouds at 6000 m is only 350 m and that this *"problem can be reduced by increasing the distance between the two cameras"* (Janeiro et al. (2012)). The combinations of camera resolution and distances used in Katai-Urban et al. (2016) (90 m, 5184×3456 pixels) and Katai-Urban et al. (2018) (90/100/130 m, 5184×3456 pixels) as well as the modeling conducted there also agree with our findings as the focus in these publications is on low clouds.

Some publications use combinations of camera resolution and distances which are not in accordance with our findings. For instance, Kassianov et al. (2005) *models* that 352×288 pixels cameras with a distance of 540 m could be feasible. We think that such a setup would only be feasible for low clouds and faces difficulties while determining the altitudes of high clouds. On the other hand, we are convinced that the setup used by Allmen and Kegelmeyer Jr (1996) (5540 m, 256×256 pixels) cannot determine low cloud heights due to the lack of overlap.

Voxel-carving approaches (Nouri et al. (2017), Kuhn et al. (2017)) model a 3-dimensional cloud form out of the different viewing geometries of the cameras. For this approach, the viewing geometries must be as different as possible, which lets larger camera distances appear more reasonable. Hence, besides the discussions on the overlap between the cameras, the findings in this study are not directly applicable to voxel carving systems. With the exception of voxel-carving, we estimate that the findings here hypothetically hold for a large variety of algorithmic approaches presented in the literature.

All-sky imager based systems can automatically measure multiple cloud heights at once, derive cloud types and cloud coverage as well as cloud motion vectors. Therefore, such low cost and robust devices might be the key meteorological instrument in the near future.

## Acknowledgements

The European Union's FP7 program under Grant Agreement no. 608623 (DNICast project) financed operations of the all-sky imagers. With funding from the German Federal Ministry for Economic Affairs and Energy within the WobaS project, all-sky imager systems were further developed.

## References

## References

Ackerman, S.A., Cox, S.K., 1981. Comparison of Satellite and All-Sky Camera Estimates of Cloud Cover during GATE. Journal of Applied Meteorology 20, 581–587. URL: https://doi.org/10.1175/1520-0450(1981)020<0581:COSAAS>2.0.CO;2, doi:10.1175/1520-0450(1981)020<0581:COSAAS>2.0.CO;2.

Allmen, M.C., Kegelmeyer Jr, W.P., 1996. The Computation of Cloud-Base Height from Paired Whole-Sky Imaging Cameras. Journal of Atmospheric and Oceanic Technology 13, 97–113. URL: https://doi.org/10.1175/1520-0426(1996)013<0097:TCOCBH>2.0.CO;2.

Andreev, M.S., Chulichkov, A.I., Emilenko, A.S., Medvedev, A.P., Postylyakov, O.V., 2014. Estimation of cloud height using ground-based stereophotography: methods, error analysis and validation. Proc. SPIE 9259, 92590N–92590N–6. URL: http://proceedings.spiedigitallibrary.org/proceeding.aspx?articleid=1974843, doi:10.1117/12.2069800.

Atsushi, T., 2004. Fatal miscommunication: English in aviation safety. World Englishes 23, 451–470. URL: https://onlinelibrary.wiley.com/doi/abs/10.1111/j.0883-2919.2004.00368.x, doi:10.1111/j.0883-2919.2004.00368.x, arXiv:https://onlinelibrary.wiley.com/doi/pdf/10.1111/j.0883-2919.2004.00368.x.

Beekmans, C., Schneider, J., Läbe, T., Lennefer, M., Stachniss, C., Simmer, C., 2016. Cloud photogrammetry with dense stereo for fisheye cameras. Atmospheric Chemistry and Physics 16, 14231–14248. URL: http://dx.doi.org/10.5194/acp-16-14231-2016, doi:10.5194/acp-16-14231-2016.

Bernecker, D., Riess, C., Christlein, V., Angelopoulou, E., Hornegger, J., 2013. Representation Learning for Cloud Classification. Springer Berlin Heidelberg, Berlin, Heidelberg. URL: http://dx.doi.org/10.1007/978-3-642-40602-7_42.

Blanc, P., Massip, P., Kazantzidis, A., Tzoumanikas, P., Kuhn, P., Wilbert, S., Schüler, D., Prahl, C., 2017. Short-Term Forecasting of High Resolution Local DNI Maps with Multiple Fish-Eye Cameras in Stereoscopic Mode. AIP Conference Proceedings 1850, 140004. URL: http://aip.scitation.org/doi/abs/10.1063/1.4984512, doi:10.1063/1.4984512.

Campbell, J.R., Peterson, D.A., Marquis, J.W., Fochesatto, G.J., Vaughan, M.A., Stewart, S.A., Tackett, J.L., Lolli, S., Lewis, J.R., Oyola, M.I., Welton, E.J., 2018. Unusually Deep Wintertime Cirrus Clouds Observed over the Alaskan Subarctic. Bulletin of the American Meteorological Society 99, 27–32. URL: https://doi.org/10.1175/BAMS-D-17-0084.1, doi:10.1175/BAMS-D-17-0084.1.

Chu, Y., Pedro, H.T., Kaur, A., Kleissl, J., Coimbra, C.F., 2017. Net load forecasts for solar-integrated operational grid feeders. Solar Energy 158, 236 – 246. URL: http://www.sciencedirect.com/science/article/pii/S0038092X17308393, doi:https://doi.org/10.1016/j.solener.2017.09.052.

Damiani, R., Zehnder, J., Geerts, B., Demko, J., Haimov, S., Petti, J., Poulos, G.S., Razdan, A., Hu, J., Leuthold, M., French, J., 2008. The Cumulus, Photogrammetric, In Situ, and Doppler Observations Experiment of 2006. Bulletin of the American Meteorological Society 89, 57–74. URL: https://doi.org/10.1175/BAMS-89-1-57, doi:10.1175/BAMS-89-1-57.

Dev, S., Lee, Y.H., Winkler, S., 2017. Color-Based Segmentation of Sky/Cloud Images From Ground-Based Cameras. IEEE Journal of Selected Topics in Applied Earth Observations and Remote Sensing 10, 231–242. URL: http://ieeexplore.ieee.org/document/7471439/, doi:10.1109/JSTARS.2016.2558474.

EKO Instruments, 2018. All Sky Imager Cloud Base Height Software ASI-16. Technical Report. EKO Instruments B.V. URL: https://media.eko-eu.com/assets/media/EKO_ASI16Manual_CloudBaseHeight_.pdf.

Fultz, A.J., Ashley, W.S., 2016. Fatal weather-related general aviation accidents in the united states. Physical Geography 37, 291–312. URL: https://doi.org/10.1080/02723646.2016.1211854, doi:10.1080/02723646.2016.1211854.

Gaumet, J.L., Heinrich, J.C., Cluzeau, M., Pierrard, P., Prieur, J., 1998. Cloud-Base Height Measurements with a Single-Pulse Erbium-Glass Laser Ceilometer. Journal of Atmospheric and Oceanic Technology 15, 37–45. URL: https://doi.org/10.1175/1520-0426(1998)015<0037:CBHMWA>2.0.CO;2, doi:10.1175/1520-0426(1998)015<0037:CBHMWA>2.0.CO;2.

Gutwin, C., Fedak, C., 2004. A comparison of fisheye lenses for interactive layout tasks, in: Proceedings of Graphics Interface 2004, Canadian Human-Computer Communications Society, School of Computer Science, University of Waterloo, Waterloo, Ontario, Canada. pp. 213–220. URL: http://dl.acm.org/citation.cfm?id=1006058.1006084.

Heinle, A., Macke, A., Srivastav, A., 2010. Automatic cloud classification of whole sky images. At-

mospheric Measurement Techniques 3, 557. URL: http://dx.doi.org/10.5194/amt-3-557-2010, doi:10.5194/amt-3-557-2010.

Hu, J., Razdan, A., Zehnder, J.A., 2009. Geometric Calibration of Digital Cameras for 3D Cumulus Cloud Measurements. Journal of Atmospheric and Oceanic Technology 26, 200–214. URL: https://doi.org/10.1175/2008JTECHA1079.1, doi:10.1175/2008JTECHA1079.1.

Hunter, D.R., 2002. Risk perception and risk tolerance in aircraft pilots. Technical Report. Federal Aviation Administration Washington DC Office of Aviation Medicine. URL: http://www.dtic.mil/dtic/tr/fulltext/u2/a407997.pdf.

Janeiro, F.M., Carretas, F., Kandler, K., Ramos, P.M., Wagner, F., 2012. Automated cloud base height and wind speed measurement using consumer digital cameras. XX IMEKO World Congr URL: http://dspace.uevora.pt/rdpc/handle/10174/5420.

Jayadevan, V.T., Rodriguez, J.J., Cronin, A.D., 2015. A new contrast-enhancing feature for cloud detection in ground-based sky images. Journal of Atmospheric and Oceanic Technology 32, 209–219. URL: https://doi.org/10.1175/JTECH-D-14-00053.1, doi:10.1175/JTECH-D-14-00053.1, arXiv:https://doi.org/10.1175/JTECH-D-14-00053.1.

Johnson, R.W., Hering, W.S., Shields, J.E., 1989. Automated Visibility & Cloud Cover Measurements with a Solid State Imaging System. Technical Report. SCRIPPS INSTITUTION OF OCEANOGRAPHY LA JOLLA CA MARINE PHYSICAL LAB. URL: http://www.dtic.mil/docs/citations/ADA216906.

Kassander, A.R., Sims, L.L., 1957. CLOUD PHOTOGRAMMETRY WITH GROUND-LOCATED K-17 AERIAL CAMERAS. Journal of Meteorology 14, 43–49. URL: https://doi.org/10.1175/0095-9634-14.1.43, doi:10.1175/0095-9634-14.1.43.

Kassianov, E., Long, C.N., Christy, J., 2005. Cloud-Base-Height Estimation from Paired Ground-Based Hemispherical Observations. Journal of Applied Meteorology 44, 1221–1233. URL: http://dx.doi.org/10.1175/JAM2277.1, doi:10.1175/JAM2277.1.

Katai-Urban, G., Eichhardt, I., Otte, V., Megyesi, Z., Bixel, P., 2018. Reconstructing atmospheric cloud particles from multiple fisheye cameras. Solar Energy 171, 171 – 184. URL: http://www.sciencedirect.com/science/article/pii/S0038092X18306017, doi:https://doi.org/10.1016/j.solener.2018.06.050.

Katai-Urban, G., Otte, V., Kees, N., Megyesi, Z., Bixel, P., 2016. STEREO RECONSTRUCTION OF ATMOSPHERIC CLOUD SURFACES FROM FISHEYE CAMERA IMAGES. International Archives of the Photogrammetry, Remote Sensing & Spatial Information Sciences

560 41. URL: https://www.int-arch-photogramm-remote-sens-spatial-inf-sci.net/XLI-B3/49/
561 2016/isprs-archives-XLI-B3-49-2016.pdf.

562 Kazantzidis, A., Tzoumanikas, P., Bais, A., Fotopoulos, S., Economou, G., 2012. Cloud detection and
563 classification with the use of whole-sky ground-based images. Atmospheric Research 113, 80–88. URL:
564 http://dx.doi.org/10.1016/j.atmosres.2012.05.005, doi:10.1016/j.atmosres.2012.05.005.

565 Kuhn, P., Bijan Nouri, S.W., Bianco, L., Vallance, L., Prahl, C., Ramirez, L., Zarzalejo, L., Schmidt, T.,
566 Yasser, Z., Vuilleumier, L., Heinemann, D., Kazantzidis, A., Wilczak, J.M., Blanc, P., Pitz-Paal, R.,
567 2018a. Vergleich und Bewertung solarer Nowcasting-Systeme, in: conexio GmbH (Ed.), Tagungsunter-
568 lagen PV-Symposium 2018. URL: http://www.pv-symposium.de/programm/tagungsunterlagen.
569 html.

570 Kuhn, P., Nouri, B., Wilbert, S., Prahl, C., Kozonek, N., Schmidt, T., Yasser, Z., Ramirez, L., Zarzalejo,
571 L., Meyer, A., Vuilleumier, L., Heinemann, D., Blanc, P., Pitz-Paal, R., 2017. Validation of an all-sky
572 imager-based nowcasting system for industrial PV plants. Progress in Photovoltaics: Research and
573 Applications 26, 608–621. URL: http://dx.doi.org/10.1002/pip.2968, doi:10.1002/pip.2968.
574 pIP-17-122.R1.

575 Kuhn, P., Wirtz, M., Killius, N., Wilbert, S., Bosch, J., Hanrieder, N., Nouri, B., Kleissl, J., Ramirez,
576 L., Schroedter-Homscheidt, M., Heinemann, D., Kazantzidis, A., Blanc, P., Pitz-Paal, R., 2018b.
577 Benchmarking three low-cost, low-maintenance cloud height measurement systems and ecmwf cloud
578 heights against a ceilometer. Solar Energy 168, 140 – 152. URL: http://www.sciencedirect.
579 com/science/article/pii/S0038092X1830183X, doi:https://doi.org/10.1016/j.solener.2018.
580 02.050. advances in Solar Resource Assessment and Forecasting.

581 Martínez-Chico, M., Batlles, F., Bosch, J., 2011. Cloud classification in a mediterranean location using
582 radiation data and sky images. Energy 36, 4055–4062. URL: http://dx.doi.org/10.1016/j.energy.
583 2011.04.043, doi:10.1016/j.energy.2011.04.043.

584 Martucci, G., Milroy, C., O'Dowd, C.D., 2010. Detection of Cloud-Base Height Using Jenoptik CHM15K
585 and Vaisala CL31 Ceilometers. Journal of Atmospheric and Oceanic Technology 27, 305–318. URL:
586 http://dx.doi.org/10.1175/2009JTECHA1326.1, doi:10.1175/2009JTECHA1326.1.

587 Massip, P., Blanc, P., Kazantzidis, A., Tzoumanikas, P., 2015. Report on algorithms for nowcasting
588 methods based on sky imagers. DNICast deliverable 3.1 URL: http://www.dnicast-project.net.

589 Mecikalski, J.R., Feltz, W.F., Murray, J.J., Johnson, D.B., Bedka, K.M., Bedka, S.T., Wimmers, A.J.,
590 Pavolonis, M., Berendes, T.A., Haggerty, J., Minnis, P., Bernstein, B., Williams, E., 2007. Aviation
591 Applications for Satellite-Based Observations of Cloud Properties, Convection Initiation, In-Flight

Icing, Turbulence, and Volcanic Ash. Bulletin of the American Meteorological Society 88, 1589–1607. URL: https://doi.org/10.1175/BAMS-88-10-1589, doi:10.1175/BAMS-88-10-1589.

Müller, R., Haussler, S., Jerg, M., 2018. The Role of NWP Filter for the Satellite Based Detection of Cumulonimbus Clouds. Remote Sensing 10. URL: http://www.mdpi.com/2072-4292/10/3/386, doi:10.3390/rs10030386.

Nguyen, D.A., Kleissl, J., 2014. Stereographic methods for cloud base height determination using two sky imagers. Solar Energy 107, 495–509. URL: http://dx.doi.org/10.1016/j.solener.2014.05.005, doi:10.1016/j.solener.2014.05.005.

Nouri, B., Kuhn, P., Wilbert, S., Prahl, C., Pitz-Paal, R., Blanc, P., Schmidt, T., Yasser, Z., Santigosa, L.R., Heinemann, D., 2017. Nowcasting of DNI Maps for the Solar Field Based on Voxel Carving and Individual 3D Cloud Objects from All Sky Images. SolarPACES 2017, to be published in AIP Conference Proceedings .

Nouri, B., Wilbert, S., Hanrieder, N., Kuhn, P., Schroedter-Homscheidt, M., Pitz-Paal, R., Zarzalejo, L., Kumar, S., Goswami, N., Shankar, R., Affolter, R., 2018. Intra-hour classification of direct normal irradiance for two sites in Spain and India. SolarPACES 2018, to be published in AIP Conference Proceedings .

Öktem, R., Prabhat, Lee, J., Thomas, A., Zuidema, P., Romps, D.M., 2014. Stereophotogrammetry of Oceanic Clouds. Journal of Atmospheric and Oceanic Technology 31, 1482–1501. URL: https://doi.org/10.1175/JTECH-D-13-00224.1, doi:10.1175/JTECH-D-13-00224.1.

Orville, H.D., Jr., A.R.K., 1961. TERRESTRIAL PHOTOGRAMMETRY OF CLOUDS. Journal of Meteorology 18, 682–687. URL: https://doi.org/10.1175/1520-0469(1961)018<0682:TPOC>2.0.CO;2, doi:10.1175/1520-0469(1961)018<0682:TPOC>2.0.CO;2.

Peng, Z., Yu, D., Huang, D., Heiser, J., Yoo, S., Kalb, P., 2015. 3d cloud detection and tracking system for solar forecast using multiple sky imagers. Solar Energy 118, 496–519. URL: http://dx.doi.org/10.1145/2554850.2554913, doi:10.1145/2554850.2554913.

Roy, J.C.E., 2016. Design and installation of a Sky-camera network and data acquisition system for intra-hour solar irradiance and photovoltaic system output forecasting. Ph.D. thesis. Murdoch University. Available online: http://researchrepository.murdoch.edu.au/id/eprint/36738/.

Savoy, F.M., Dev, S., Lee, Y.H., Winkler, S., 2017. Stereoscopic cloud base reconstruction using high-resolution whole sky imagers , 141–145URL: https://pdfs.semanticscholar.org/d20d/5f1c11b3903bf07d12a94f6be8b98dbc840c.pdf, doi:10.1109/ICIP.2017.8296259.

Schmidt, M., Heller, C.M.A., Mayer, O.G., Zettl, M., Gonzalez, O.I.S., Hernandez, Y.N.M., Lynass, M.R., Serra, E.B., Hartung, M., 2015. Methods and systems for predicting cloud movement. US Patent 9,007,460.

Seiz, G., Shields, J., Feister, U., Baltsavias, E., Gruen, A., 2007. Cloud mapping with ground-based photogrammetric cameras. International Journal of Remote Sensing 28, 2001–2032. URL: http://dx.doi.org/10.1080/01431160600641822, doi:10.1080/01431160600641822.

Singh, S., Rondinelli, M., Herman, H., 2006. System and method for panoramic imaging. US Patent 7,058,239.

Stefferud, K., Kleissl, J., Schoene, J., 2012. Solar forecasting and variability analyses using sky camera cloud detection and motion vectors, in: 2012 IEEE Power and Energy Society General Meeting, pp. 1–6. doi:10.1109/PESGM.2012.6345434.

Strachey, R., Whipple, G.M., 1891. Cloud photography conducted under the Meteorological Council at the Kew Observatory. Proceedings of the Royal Society of London 49, 467–480. URL: http://rspl.royalsocietypublishing.org/content/49/296-301/467.short, doi:10.1098/rspl.1890.0117, arXiv:http://rspl.royalsocietypublishing.org/content/49/296-301/467.full.pdf+html.

Tapakis, R., Charalambides, A., 2013. Equipment and methodologies for cloud detection and classification: A review. Solar Energy 95, 392–430. URL: http://dx.doi.org/10.1016/j.solener.2012.11.015, doi:10.1016/j.solener.2012.11.015.

Taravat, A., Frate, F.D., Cornaro, C., Vergari, S., 2015. Neural networks and support vector machine algorithms for automatic cloud classification of whole-sky ground-based images. IEEE Geoscience and Remote Sensing Letters 12, 666–670. URL: https://doi.org/10.1109/LGRS.2014.2356616, doi:10.1109/LGRS.2014.2356616.

Tohsing, K., Schrempf, M., Riechelmann, S., Schilke, H., Seckmeyer, G., 2013. Measuring high-resolution sky luminance distributions with a CCD camera. Appl. Opt. 52, 1564–1573. URL: http://ao.osa.org/abstract.cfm?URI=ao-52-8-1564, doi:10.1364/AO.52.001564.

Tohsing, K., Schrempf, M., Riechelmann, S., Seckmeyer, G., 2014. Validation of spectral sky radiance derived from all-sky camera images - a case study. Atmospheric Measurement Techniques 7, 2137–2146. URL: http://www.atmos-meas-tech.net/7/2137/2014/, doi:10.5194/amt-7-2137-2014.

Tzoumanikas, P., Nikitidou, E., Bais, A., Kazantzidis, A., 2016. The effect of clouds on surface solar irradiance, based on data from an all-sky imaging system. Renewable Energy 95, 314 – 322. URL: http://www.sciencedirect.com/science/article/pii/S0960148116303305, doi:https://doi.org/10.1016/j.renene.2016.04.026.

Urquhart, B., Chow, C.W., Nguyen, D., Kleissl, J., Sengupta, M., Blatchford, J., Jeon, D., 2012. Towards intra-hour solar forecasting using two sky imagers at a large solar power plant. Proceedings of the American Solar Energy Society, Denver, CO, USA URL: https://ases.conference-services.net/resources/252/2859/pdf/SOLAR2012_0791_full%20paper.pdf.

de WA, W., 1885. The Heights of Clouds. Nature 32, 630–631. URL: http://www.nature.com/nature/journal/v32/n835/abs/032630b0.html, doi:doi:10.1038/032630b0.

Wiegmann, D.A., Goh, J., O'Hare, D., 2002. The role of situation assessment and flight experience in pilots' decisions to continue visual flight rules flight into adverse weather. Human Factors 44, 189–197. URL: https://doi.org/10.1518/0018720024497871, doi:10.1518/0018720024497871. pMID: 12452267.

Xia, M., Lu, W., Yang, J., Ma, Y., Yao, W., Zheng, Z., 2015. A hybrid method based on extreme learning machine and k-nearest neighbor for cloud classification of ground-based visible cloud image. Neurocomputing 160, 238 – 249. URL: http://www.sciencedirect.com/science/article/pii/S092523121500171X, doi:https://doi.org/10.1016/j.neucom.2015.02.022.